ARTICLE TYPE

Cite this: DOI: 00.0000/xxxxxxxxxx

Direct Measurement of Lighthill's Energetic Efficiency of a Minimal Magnetic Microswimmer†

Carles Calero,[‡a,b] José García-Torres,[‡a,b], Antonio Ortiz-Ambriz,[a,b] Francesc Sagués,[c,b], Ignacio Pagonabarraga,[a,d,e] and Pietro Tierno [a,b,e*]

Received Date
Accepted Date

DOI: 00.0000/xxxxxxxxxx

The realization of artificial microscopic swimmers able to propel in viscous fluids is an emergent research field of fundamental interest and vast technological applications. For certain functionalities, the efficiency of the microswimmer in converting the input power provided through an external actuation into propulsive power output can be critical. Here we use a microswimmer composed by a self-assembled ferromagnetic rod and a paramagnetic sphere and directly determine its swimming efficiency when it is actuated by a swinging magnetic field. Using fast video recording and numerical simulations we fully characterize the dynamics of the propeller and identify the two independent degrees of freedom which allow its propulsion. We then obtain experimentally the Lighthill's energetic efficiency of the swimmer by measuring the power consumed during propulsion and the energy required to translate the propeller at the same speed. Finally, we discuss how the efficiency of our microswimmer could be increased upon suitable tuning of the different experimental parameters.

The realization of faster and smaller micro/nanopropellers is an active topic with direct applications in the emerging fields of drug delivery[1–3], microsurgery[4,5] and lab-on-a-chip technology[6,7]. The main challenge arises from the low Reynolds number regime in which these microppellers operate, where viscous forces dominate over inertial ones and the Stokes equation becomes time reversible. Thus, in order to attain propulsion, these prototypes should avoid reciprocal motion, namely periodic backward and forward displacement. As described by Purcell, this condition can be satisfied by a minimum of two independent degrees of freedom, when their change in time describes a finite area in the parameter space[8].

Recent years have witnessed a variety of theoretical propositions[9], and a number of experimental advances[10] which have provided multiple microppeller prototypes based on different propulsion mechanisms, including chemical reactions[11,12], magnetic[13–16] or light fields[17,18]. Most of these prototypes have been characterized and compared mainly in terms of their achievable speed, a simple observable that can be calculated directly from particle tracking. However, choosing the correct propulsion scheme for a specific task requires a suitable measure of the propeller efficiency not limited to the sole speed. The control of swimming efficiency is of paramount importance both in artificial microswimmers to, e.g. avoid excessive heating due to dissipation, and in microorganisms to optimize energy release[19].

In 1975 Lighthill quantified the swimmer efficiency in converting input energy to thrust power through a single parameter e, which compares the external power $\langle\Phi\rangle$, required to induce a mean velocity V in a medium of viscosity η, to the power needed to rigidly drag the swimmer at the same speed with an external force F_{drag}[20],

$$e = \frac{F_{drag} V}{\langle\Phi\rangle} \tag{1}$$

Although other measures of the efficiency have been proposed[19,21], especially to account for collective ciliary motions, the Lighthill energetic efficiency remains the standard measure to account for swimming efficiency of single propellers at the microscale. This parameter has been employed in different theoretical works to analyze the performance of simple artificial designs

[a] Departament de Física de la Matèria Condensada, Universitat de Barcelona, 08028 Barcelona, Spain.
[b] Institut de Nanociència i Nanotecnologia, Universitat de Barcelona, 08028 Barcelona , Spain.
[c] Departament de Ciència de Materials i Química Física, Universitat de Barcelona, Barcelona, Spain.
[d] CECAM, Centre Européen de Calcul Atomique et Moléculaire, École Polytechnique Fédérale de Lasuanne, Batochime, Avenue Forel 2, Lausanne, Switzerland.
[e] Universitat de Barcelona, Institute of Complex Systems (UBICS), Universitat de Barcelona, 08028 Barcelona, Spain.
* E-mail: ptierno@ub.edu

† Electronic Supplementary Information (ESI) available: Two experimental videos (.WMF) showing the dynamics of the nanorod-colloid microppeller played at different speed. See DOI: 00.0000/00000000.

‡These authors contributed equally to this work.

like three-link flagella[22–24], three-sphere swimmers[25], squirmers[26], necklace-like propellers[27] and undulating magnetic systems[28]. However, to date Lighthill's efficiency has been only experimentally estimated in few biological systems[29,30], where the complex flagellar dynamics precludes the possibility to directly determine the relevant degrees of freedom of the microswimmer, and indirect methods such as optical tweezers, are used.

In this article we directly measure the energetic Lighthill efficiency of a minimal magnetic microswimmer cyclically actuated by an external magnetic field. The microswimmer is composed by a ferromagnetic nanorod and a paramagnetic microsphere which self-assemble due to magnetic dipolar interactions. The pair is subjected to a swinging magnetic field that forces the rod to tilt and to slide at the surface of the microsphere. Such an actuating field would not induce propulsion for a single body swimmer in a viscous fluid, unless composed by a flexible tail[31]. The simplicity of the microswimmer allows us to show that its locomotion is enabled by only two independent degrees of freedom, which are experimentally identified and characterized. The precise measurement of the microswimmer dynamics allows for a direct, accurate and systematic measurement of its energetic Lighthill efficiency. By combining real space/time experiments with theory and numerical simulations, we determine speed and efficiency over a large range of frequencies and amplitudes. We will first describe the microswimmer and indicate how we exploit its simplicity to describe its behavior both experimentally and theoretically. We exploit subsequently this detailed control to quantify its efficiency and characterize its regime of motion.

Our hybrid microswimmer is composed by a spherical paramagnetic particle of radius $R = 1.5\mu$m and a ferromagnetic Nickel nanorod that is synthesized via template-assisted electrodeposition. The latter has a length of $L = 3\mu$m, a diameter of $D = 400$nm and displays a permanent magnetic moment along its long axis, $m_n = 3.7 \cdot 10^{-11}\mathrm{Am}^{-2}$. In contrast, the spherical particle is characterized by a magnetic volume susceptibility $\chi = 0.21$, and under an external field $\boldsymbol{B}$ acquires an induced moment $\boldsymbol{m}_p = 4\pi R^3 \chi \boldsymbol{B}/(3\mu_0)$ which points along the field direction, being $\mu_0 = 4\pi \cdot 10^{-7}\mathrm{Hm}^{-1}$. Both elements are dispersed in highly deionized water and allowed to sediment above a glass substrate, which is placed at the center of a set of orthogonal coils arranged on the stage of a brightfield optical microscope, more details are in the Material and Methods section. To further understand the experimental data, we perform numerical simulations of a simple theoretical model of the microswimmer which captures the geometry of the particles and considers their mutual magnetic and hydrodynamic interactions, see Materials and Methods section for more details.

We actuate our prototype by using a swinging magnetic field composed by an oscillating component B_y with frequency ν and a perpendicular, static field B_x, $\boldsymbol{B} \equiv [B_x, B_y \sin(2\pi\nu t)]$. The effect of the applied field on the relative displacement of the two elements during a half-cycle, $t \in [1/(2\nu), 3/(2\nu)]$, is shown in Fig.1(a). Initially, both the permanent, m_n, and the induced, m_p, moments are aligned with the field direction, $B_x, B_y > 0$. As B_y oscillates, m_p follows instantaneously the external field. The nanorod rotates an angle θ about the contact point with the paramagnetic particle

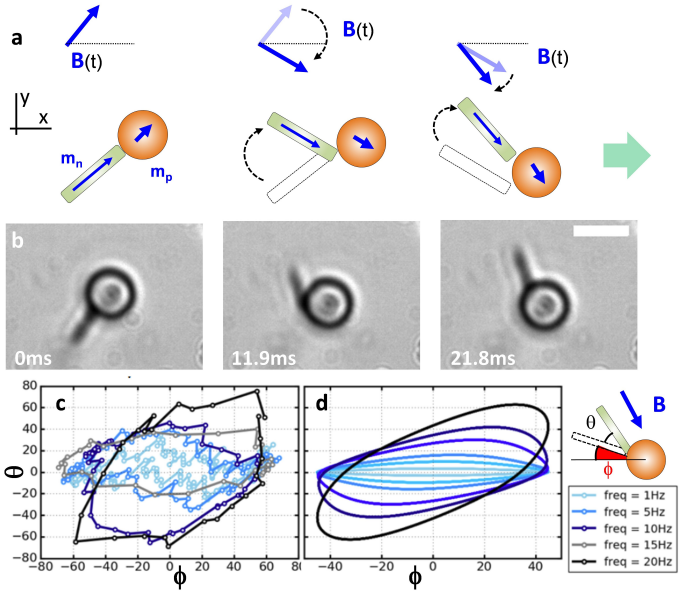

Fig. 1 (a) Sequence of schematics showing the colloid-nanorod pair subjected to the swinging magnetic field $\boldsymbol{B}(t)$ during half-cycle, m_n and m_p denote, respectively, the permanent and the induced moments of the nanorod and the colloid. (b) Corresponding microscope images showing relative movement of the pair during half cycle. The pair is propelled by a field with frequency $\nu = 20$Hz and amplitudes $B_x = 2.15$mT, $B_y = 2.74$mT and recorded at 504 fps, see corresponding VideoS1 and VideoS2 in the Supporting Information. The scale bar is 5μm. (c,d) Cycles in the (ϕ, θ) plane at different frequencies of the applied field for experiments (c) and numerical simulation (d). The small schematic on the right provides the definition of the rotational angle of the nanorod (θ), and the angle between the x-axis and the contact point between the nanorod and the particle, (ϕ)

due to the torque exerted by the field. Simultaneously, the attractive dipolar interaction between the pair forces the rod to slide over the particle surface to align with m_p, minimizing the magnetic energy of the pair. Such sliding motion can be characterized by a second degree of freedom ϕ (see Fig 1), which represents the angle between the x-axis and the contact point between the tip of the rod and the particle. The uncoupled rotation and sliding motions are able to break the time-reversal symmetry of the flow, leading to the microswimmer net translation. This mechanism is observed in our numerical simulations and demonstrated experimentally in Fig.1(b), where the pair moves with the microsphere in front of it for these geometric parameters. Therefore, the propulsion of the microswimmer is allowed by the two decoupled rotational modes and it does not require the presence of a bounding wall, as opposed to the mechanism reported in Ref.[32].

We record high frame-rate videos to directly measure the two angular degrees of freedom (ϕ, θ). The non-reciprocity of the cyclical motion is evident from the trajectories in the parameter space (ϕ, θ) shown in Fig.1(c) for experiments, and in Fig.1(d) for simulations. Indeed, the trajectories follow different paths in the first and second half-cycles of the actuating field $\mathbf{B}(t)$, describing a closed asymmetric region. As the frequency of the field is reduced, the rotation and sliding motions of the rod become more

synchronized and the deformation approaches reciprocity. As a result, the first and second half-cycles of the trajectories shown in Figs.1(c,d) approach one another, coming close to a straight line for the lowest frequencies.

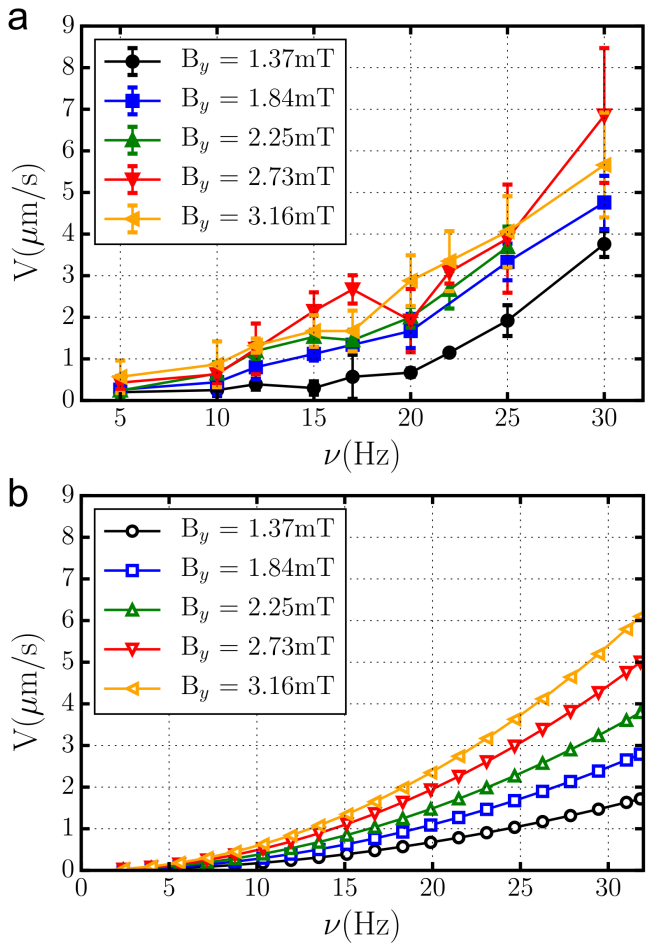

Fig. 2 (a,b) Velocity of the magnetic propeller as a function of the frequency ν for different amplitudes of the applied field from experiments (a) and simulations (b). In both cases the static field component is kept constant to $B_x = 2.15$mT.

Fig.2(a) displays the resulting propulsion speed as a function of frequency and amplitude B_y of the driving magnetic field, with fixed longitudinal component $B_x = 2.15$mT. The experimental curves follow the same trends obtained in numerical simulations of the system shown in Fig. 2(b). Both set of results demonstrate that the propeller velocity increases with the frequency of the transverse oscillating field, consistent with the observed increase in the area enclosed by the (ϕ,θ) trajectories.

The microswimmer displacement is determined by the motion of the contact point of the rod and the sphere. This motion can be resolved using resistive force theory[33] and Stokes's law to account for the overdamped interaction of the rod and spherical colloid with the fluid, respectively. In this formulation, the propulsion speed is controlled by three dimensionless parameters, the ratio between the particles sizes $\delta = R/L$, $\alpha_{ind} = \mu_0 m_n/(R^3 B_x)$ that compares the magnetic field induced by the ferromagnet on the paramagnetic particle with the external field, and the susceptibility χ of the paramagnetic particle. The propeller dynamics can be solved perturbatively[24,28,34] for a weak oscillating transverse field, $B_y/B_x \equiv \varepsilon \ll 1$.

The averaged propeller velocity V, to leading order in ε reads

$$V/V_0 = \varepsilon^2 \frac{b_1(\nu/\nu_0)^2}{a_4(\nu/\nu_0)^4 + a_2(\nu/\nu_0)^2 + a_0} + \mathscr{O}(\varepsilon^4), \qquad (2)$$

where $V_0 = R\nu_0$, and $\nu_0 = \frac{9B_x m_n}{\pi\eta L^3}$ is a characteristic frequency of the problem. b_1, a_0, a_2, a_4 are coefficients which depend on δ, α_{ind} and χ (see Supporting Information). Eq. 2 shows a non-monotonic dependence on frequency, leading to an optimal propulsion at $\nu_V^{max} = \nu_0(a_0/a_4)^{1/4}$. For the experimentally relevant frequency range, one can approximate $V/V_0 = \varepsilon^2(b_1/a_0)(\nu/\nu_0)^2$, exhibiting a quadratic dependence on the frequency of the transverse field, consistent with the results obtained both experimentally and computationally, see Fig. 2. Although the experiments need to be performed in conditions where $B_y/B_x \approx 1$ to be able to track in detail the motions of the magnetic particles, the leading order solutions of the theoretical model in ε, Eq. 2 (and Eq. 3 below), provide insights on the functional form and relevant parameters of the problem. The perturbative analytical solutions, Eq. 2, are validated by comparing with numerical simulations of the model, exhibiting good agreement even for $B_y/B_x \approx 1$.

In order to extract the Lighthill efficiency, e, from the experimental data, we measured independently the external power P_B exerted on the system, and the equivalent power P required to translate the propeller. Since the only work exerted by the external field is due to the torque on the ferromagnetic rod (which is then partly transferred to the sliding motion), we can express the instantaneous external power as $P_B(t) = \boldsymbol{\tau}_B(t)\cdot\dot{\boldsymbol{\alpha}}$, being $\boldsymbol{\tau}_B(t) = \mathbf{m}_n(t)\times\mathbf{B}(t)$ the instantaneous torque applied on the rod, and $\dot{\alpha}$ the rod angular velocity. The average power in one period of the magnetic field is given by $\bar{P}_B = \nu\int_0^{1/\nu} P_B(t)dt$. This quantity is determined from the orientation and angular velocity of the rod at each instant of time, see Materials and Methods for more details. We calculate the phase between $\mathbf{m}_n$ and $\mathbf{B}$ by coupling to a light emitting diode the signal of the ac current flowing through the Helmholtz coils. The power needed to rigidly drag the swimmer at a given speed v is obtained by using controlled magnetic gradients, $P = v\mathbf{m}_n\cdot\nabla\mathbf{B}$. The resulting experimental data are shown in Fig.3(a), where e is measured in the frequency range $\nu \in [10,30]$Hz and at different amplitudes B_y with fixed $B_x = 2.15$mT. In the efficiency calculation we neglect the contribution due to the rotational motion of the paramagnetic sphere. From the analysis of the experimental videos we find that that such rotation was $\sim 5^\circ$ and its contribution negligible respect to the rotation of the rod.

The perturbative solution of the dynamical model provides an analytical expression for the Lighthill efficiency at small driving amplitudes ε,

$$e = \varepsilon^2 \frac{n_2(\nu/\nu_0)^2}{d_6(\nu/\nu_0)^6 + d_4(\nu/\nu_0)^4 + d_2(\nu/\nu_0)^2 + d_0} + \mathscr{O}(\varepsilon^4), \qquad (3)$$

which reduces to $e = \varepsilon^2(n_2/d_0)(\nu/\nu_0)^2$ in the range of experimen-

tally accessible frequencies. The coefficients n_2, d_6, d_4 and d_2 are given by the parameters of the problem $\delta, \alpha_{ind}, \chi$. Figs. 3 show a qualitative agreement between the measured values of the Lighthill efficiency and the predictions from simulations and the dynamical model.

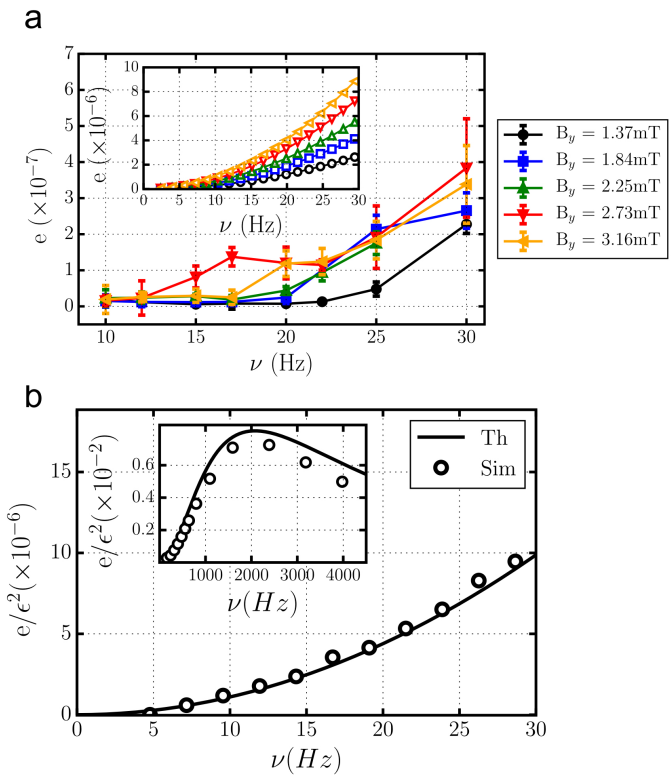

Fig. 3 (a) Propeller efficiency e versus frequency ν of the swinging field for different amplitudes B_y as measured in the experiments. Inset shows results for the efficiency obtained from simulations. (b) Normalized efficiency e/ε^2 versus frequency ν as obtained from the theoretical model (solid line) and simulations (dots). Inset shows e/ε^2 for a wide range of frequencies to visualize a peak at $\nu_e^{max} = 1776$Hz.

We note that the quantitative discrepancies between the experiments and the computational predictions can be attributed to different factors. Specifically, paramagnetic colloids, composed of magnetic domains in a non-magnetic matrix, can present a residual magnetic anisotropy[35]. As a result, the rotation of the spherical colloid due to the interaction with the external field and the field induced by the ferromagnetic rod can contribute to the dissipation, without affecting the overall swimmer propulsion. In addition, as a consequence of such interaction, the ferromagnetic rod could acquire a higher dephasing with the external field, resulting in a larger input power. Other factors such as the interaction with the surface and the action of gravity on the couple could also be a source of discrepancy.

Eq. 3 predicts the existence of an optimal efficiency at a frequency ν_e^{max} (~ 1776 Hz for the parameters of the experimental system), where the efficiency is over three orders of magnitude higher than the one measured at the experimentally accessible frequencies (see inset of Fig. 3). Additionally, the analytical model allows for an optimal design of the microswimmer that maximizes its efficiency for a given field $\mathbf{B}(t)$. While the efficiency is not very sensitive to δ and α_{ind}, it exhibits a strong dependence on the susceptibility of the paramagnetic particle (see Supporting Information). Indeed, Eq. 3 predicts that the efficiency of the microswimmer has a maximum for a susceptibility $\chi_{max} \approx 0.32$ if one keeps the other parameters of the microswimmer constant, for which the efficiency is more than an order of magnitude higher. Note that for $\chi \gg 1$, the phase difference between the rotation and sliding motions of the ferromagnetic rod vanishes generating a reciprocal motion. On the other hand, for $\chi \ll 1$ the sliding motion does not occur, leaving only one independent degree of freedom and thus no propulsion. Note also that the frequency of maximum efficiency is inversely proportional to the viscosity of the solvent, which provides a possible route to optimize the efficiency of the swimmer.

In conclusion, we have determined the Lighthill energetic efficiency of a minimal self-assembled microswimmer composed by a paramagnetic microsphere and a ferromagnetic nanorod, and have developed a theoretical scheme that captures the essential dynamics of the system. The simplicity of the synthetic microswimmer allows a quantitative and precise measurement of its efficiency, showing a value smaller than flexible magnetic swimmers[?] but larger than other artificial non-propelling engines[36]. We show that the efficiency of the microswimmer is much more sensitive to the internal degrees of freedom, which are not relevant to determine its propulsion speed. The theoretical study has shown the existence of an optimal efficiency, which is three orders of magnitude larger than the one obtained experimentally. While the peak efficiency could be observed only in the model given the experimental limitations, we show that it could be controlled by varying the field parameters or the magnetic susceptibility of the paramagnetic colloid. The realization of minimal, artificial prototypes that avoid the complexity of biological systems and that can be controlled through their independent degrees of freedom, is still an open challenge in the field, in spite of the amount of theoretical propositions. More in general, when compared to other prototypes driven by external fields, magnetic microswimmers have the advantage of being easily controlled and steered trough the fluid without altering the composition of the dispersing medium, all features that make them rather appealing for practical applications. Finally, the possibility to characterize the swimming efficiency of nano/micro propellers in terms of the constituent degrees of freedom represent a key issue in many technological contexts[?] .

Conflicts of interest

There are no conflicts to declare'.

Acknowledgements

This work has received funding from the Horizon 2020 research and innovation programme, Grant Agreement No. 665440. F.S. acknowledges support from MINECO under project FIS2016-C2-1-P AEI/FEDER-EU. I.P. acknowledges support from MINECO under project FIS2015-67837-P and Generalitat de Catalunya under project 2017SGR-884 and SNF Project No. 200021-175719. P.T.

acknowledges the European Research Council (ENFORCE, No. 811234), MINECO (FIS2016-78507-C2-2-P, ERC2018-092827) and Generalitat de Catalunya under program "Icrea Academia".

Materials and Methods

Experimental System and Methods

The Ni nanorods are synthesized by template-assisted electrodeposition from a single electrolyte, $0.5\text{mol}\cdot\text{dm}^{-3}$ $NiCl_2$ solution (Sigma Aldrich), prepared with distilled water treated with a Millipore (Milli Q system). The electrosynthesis was conducted potentiostatically using a microcomputer-controlled potentiostat/galvanostat Autolab with PGSTAT30 equipment, GPES software and a three electrode system. A polycarbonate (PC) membrane with pore diameter ~ 400nm (Merck-MilliPore) and sputter-coated with a gold layer on one side to make it conductive is used as the working electrode. The reference and the counter electrodes are a Ag/AgCl/KCl ($3\text{mol}\cdot\text{dm}^{-3}$) electrode and a platinum sheet respectively. After synthesis, the Ni nanorods are released from the membrane by first removing the gold layer with a I_2/I^- aqueous solution, and then by wet etching of the PC membrane in $CHCl_3$. Nanorods are then subsequently washed with chloroform (10 times), chloroform-ethanol mixtures (3 times), ethanol (2 times) and deionised water (5 times). Finally, sodium dodecyl sulphate (Sigma Aldrich) is added to disperse nanorods. The typical length of the fabricated Ni nanorods used in this study is around $L = 3\mu$m. Structural and morphological analysis were carried out with scanning and high-resolution transmission electron microscopes. The permanent moment of the nanorod is measured by following its orientation under a static magnetic field, as described in previous works[37,38]. The value obtained for the magnetic moment of the ferromagnetic rod is $m_n = 3.7\times10^{-11}\text{Am}^{-2}$.

The spherical colloids used are paramagnetic microspheres with radius $R = 1.5\mu$m, $\sim 15\%$ iron oxide content and surface carboxylic groups (ProMag PMC3N, Bang Laboratories). The particles are characterized by a magnetic volume susceptibility equal to $\chi = 0.21$, as measured in separate experiments[32]. The particles and the nanorods are dispersed in highly deionized water (MilliQ, Millipore) and allowed to sediment above a glass substrate. The substrate is placed in the center of five orthogonal coils arranged on the stage of a light microscope (Eclipse Ni, Nikon), equipped with a Nikon $100\times$ objective with 1.3NA. The coils are connected to a wave generator (TGA1244, TTi) feeding a power amplifier (IMG AMP-1800). The particle dynamics are recorded with a CCD camera (scA640-74fc, Basler) working at around 75 frames per second (fps), with a CMOS camera (MQ003MG-CM, Ximea) working at 500 fps, or in color at 325 fps (acA640-750uc, Basler).

Measurement of the phase of the field.

To measure the phase between the instantaneous value of the applied field and the orientation of the propeller, we modify the experimental set-up by introducing two LEDs to the optical path, just above the observation objective. The two LEDs are connected in an anti-parallel configuration to an alternate current (AC) voltage source, which is produced by the same waveform generator that powers the magnetic coil system. We use a phase lock program to synchronize the oscillations coming from the two signals. In this configuration, the green LED emits light during the positive cycle of the applied field, while the red LED emits on the negative one. The tube lens of the objective allows to distribute the colored light over the whole sample view. Even if the transmitted intensity appears as relatively small, it can be distinguished from the experimental image. From the color video in RGB format, we calculate the average value of all the pixels in the red and in the green channels as a function of time.

We then perform a least squares fit using the function $f(t) = A + \frac{B}{2}(\sin(2\pi ft+\phi)+|\sin(2\pi ft+\phi)|)$ from which we extract the phase ϕ, being A and B two amplitudes. The value of ϕ allows us to calculate an instantaneous value of the field for each frame. Further, we track three points of the swimmer using the public program ImageJ (National Institutes of Health). These points are the outermost tip of the nanorod, the point of contact between the nanorod and the colloidal particle, and the center of the colloidal particle. From these three points, we extract the relative angles, and using the instantaneous direction of the applied field $\mathbf{B}$, we have all the information over the different degrees of freedom involved.

Numerical simulations

The paramagnetic particle is modeled as a spherical bead of radius R with an induced magnetic moment $\boldsymbol{m}_p$ located in its center. The ferromagnetic rod is described as a group of N equally spaced spherical beads of diameter D along a straight line. Every bead carries a fixed magnetic moment $\boldsymbol{m}_n/N$ directed along the axis of the rod. The external magnetic field exerts a torque on the ferromagnet $\boldsymbol{\tau}_B = \boldsymbol{m}_n \times \boldsymbol{B}$, which is implemented as an artificial force pair applied perpendicular to the axis of the rod. The paramagnetic particle and the ferromagnetic rod interact through magnetic dipolar interactions, which are calculated as a sum of dipolar interactions between the paramagnetic sphere and the N beads composing the ferromagnetic rod. In addition, the spherical beads composing the swimmer interact with other beads and with the bounding plane at $z = 0$ through short ranged steric interactions, which are described using the Weeks-Chandler-Andersen (WCA) potential[?] . Such interactions provide the beads with extension and prevent overlaps.

Due to the dimensions of the swimmer we assume that its dynamics is overdamped and governed by the hydrodynamic drag with the viscous fluid. The interaction of bead i of the microswimmer with the viscous fluid is given by the hydrodynamic friction force

$$\mathbf{F}_{H,i} = -\gamma_i(\mathbf{v}_i - \mathbf{u}(\mathbf{r}_i))\,, \tag{4}$$

where γ_i is the bead's friction coefficient, $\mathbf{v}_i$ its velocity, and $\mathbf{u}(\mathbf{r}_i)$ is the induced fluid flow at the bead's position. The flow field $\mathbf{u}(\mathbf{r})$ is generated by the action of the net (non hydrodynamic) forces on the different elements of the microswimmer, which is treated in the far field approximation. In fact, we approximate the hydrodynamic behavior of the particles composing the microswimmer

to that of point particles, which gives

$$\mathbf{u}(\mathbf{r}_i) = \frac{1}{8\pi\eta} \sum_j G(\mathbf{r}_i;\mathbf{r}_j) \cdot \mathbf{F}_j \,. \tag{5}$$

Here, $\mathbf{F}_j$ is the non-hydrodynamic force acting on particle j, η is the viscosity of the fluid, and $G(\mathbf{r}_i;\mathbf{r}_j)$ is the Green's function of the Stokes equation. We have considered both the case of an unbound fluid, for which we use the Oseen tensor $G^{Oseen}(\mathbf{r}_i;\mathbf{r}_j)$, and also the case with a no-slip, flat and infinite boundary for the fluid flow, for which we use the Blake tensor[39] $G^{Blake}(\mathbf{r}_i;\mathbf{r}_j)$. The actuation on our microswimmer by the applied external fields dominates over thermal effects ($\mathbf{m}_n B \gg k_B T$). For this reason, our numerical simulations do not consider the effect of temperature on the dynamics of the magnetic couple.

The dynamics of the swimmer evolves following Newton's equations of motion, which are solved using a Verlet algorithm adapted for cases with forces which depend on the velocity[40].

Notes and references

1 L. Zhang, T. Petit, Y. Lu, B. E. Kratochvil, K. E. Peyer, R. Pei, J. Lou and B. J. Nelson, *ACS Nano*, 2010, **4**, 6228.
2 K. E. Peyer, L. Zhang and B. J. Nelson, *Nanoscale*, 2013, **5**, 1259–1272.
3 W. Gao and J. Wang, *Nanoscale*, 2014, **6**, 10486–10494.
4 B. J. Nelson, I. K. Kaliakatsos and J. J. Abbott, *Annu. Rev. Biomed. Eng.*, 2010, **12**, 55.
5 K. E. Peyer, L. Zhang and B. J. Nelson, *Nanoscale*, 2013, **5**, 1259.
6 S. Sanchez, A. A. Solovev, S. M. Harazim and O. G. Schmidt, *J. Am. Chem. Soc.*, 2011, **133**, 701.
7 J. Li, O. E. Shklyaev, T. Li, W. Liu, H. Shum, I. Rozen, A. C. Balazs and J. Wang, *Nano Lett.*, 2015, **15**, 7077.
8 E. M. Purcell, *Am. J. Phys.*, 1977, **45**, 3.
9 M. C. Marchetti, J. F. Joanny, S. Ramaswamy, T. B. Liverpool, J. Prost, M. Rao and R. A. Simha, *Rev. Mod. Phys.*, 2013, **85**, 1143–1189.
10 C. Bechinger, R. Di Leonardo, H. Löwen, C. Reichhardt, G. Volpe and G. Volpe, *Rev. Mod. Phys.*, 2016, **88**, 045006.
11 W. F. Paxton, K. C. Kistler, C. C. Olmeda, A. Sen, S. K. S. Angelo, Y. Cao, T. E. Mallouk, P. E. Lammert and V. H. Crespi, *J. Am. Chem. Soc.*, 2004, **126**, 13424.
12 J. R. Howse, R. A. L. Jones, A. J. Ryan, T. Gough, R. Vafabakhsh and R. Golestanian, *Phys. Rev. Lett.*, 2007, **99**, 048102.
13 P. Tierno, R. Golestanian, I. Pagonabarraga and F. Sagués, *Phys. Rev. Lett.*, 2008, **101**, 218304.
14 L. Zhang, J. J. Abbott, L. Dong, K. E. Peyer, B. E. Kratochvil, H. Zhang, C. Bergeles and B. J. Nelson, *Nano Lett.*, 2009, **9**, 3663.
15 A. Snezhko, M. Belkin, I. S. Aranson and W.-K. Kwok, *Phys. Rev. Lett.*, 2009, **102**, 118103.
16 P. Fischer and A. Ghosh, *Nanoscale*, 2011, **3**, 557.
17 G. Volpe, I. Buttinoni, D. Vogt, H.-J. Kummerer and C. Bechinger, *Soft Matter*, 2011, **7**, 8810.
18 S. Palagi, A. G. Mark, S. Y. Reigh, K. Melde, T. Qiu, H. Zeng, C. Parmeggiani, D. Martella, A. Sanchez-Castillo, N. Kapernaum, F. Giesselmann, D. S. Wiersma, E. Lauga and P. Fischer, *Nat. Mater.*, 2016, **15**, 647.
19 N. Ostermana and A. Vilfan, *Proc. Natl Acad. Sci. USA*, 2011, **108**, 15727.
20 J. Lighthill, *Mathematical Biofluiddynamics*, SIAM, RegionalConference Series in Applied Mathematics, 1975.
21 A. Shapere and F. Wilczek, *J. Fluid Mech.*, 1989, **198**, 587.
22 L. E. Becker, S. A. Koehler and H. A. Stone, *J. Fluid Mech.*, 2003, **490**, 15.
23 E. Passov and Y. Ora, *Eur. Phys. J. E*, 2012, **35**, 78.
24 O. Wiezel and Y. Or, *Proc. R. Soc. A*, 2016, **472**, 20160425.
25 R. Golestanian and A. Ajdari, *Phys. Rev. E*, 2008, **77**, 036308.
26 K. Ishimoto and E. A. Gaffney, *Phys. Rev. E*, 2014, **90**, 012704.
27 O. Raz and A. M. Leshansky, *Phys. Rev. E*, 2008, **77**, 055305.
28 E. Gutman and Y. Or, *Phys. Rev. E*, 2016, **93**, 063105.
29 S. Chattopadhyay, R. Moldovan, C. Yeung and X. L. Wu, *Proc. Natl Acad. Sci. USA*, 2006, **103**, 13712.
30 G. Li and J. X. Tang, *Biophys. J.*, 2006, **91**, 2726.
31 R. Dreyfus, J. Baudry, M. L. Roper, M. Fermigier, H. A. Stone and J. Bibette, *Nature*, 2005, **437**, 862.
32 J. García-Torres, C. Calero, F. Sagués, I. Pagonabarraga and P. Tierno, *Nat. Comm.*, 2018, **9**, 1663.
33 S. Kim and S. J. Karrila, *Microhydrodynamics: principles and selected applications*, Courier Corporation, 2013.
34 E. Gutman and Y. Or, *Phys. Rev. E*, 2014, **90**, 013012.
35 X. J. A. Janssen, A. J. Schellekens, K. van Ommering, L. J. van Ijzendoorn and M. J. Prins, *Biosens. Bioelectron.*, 2009, **24**, 1937.
36 F. Schmidt, A. Magazzù, A. Callegari, L. Biancofiore, F. Cichos and G. Volpe, *Phys. Rev. Lett.*, 2018, **120**, 068004.
37 F. Martinez-Pedrero, A. Cebers and P. Tierno, *Phys. Rev. Applied*, 2016, **6**, 034002.
38 F. Martinez-Pedrero, A. Cebers and P. Tierno, *Soft Matter*, 2016, **12**, 3688–3695.
39 J. R. Blake, *Proc. Camb. Philos. Soc.*, 1971, **70**, 303.
40 A. G. Bailey, C. P. Lowe, I. Pagonabarraga and M. C. Lagomarsino, *Phys. Rev. E*, 2009, **80**, 046707.